New data for total ³He(γ, p)D and ³He(γ, pp)n cross sections compared to current theory

S. Naito,[1,*] Y. Nagai,[1,†] T. Shima,[1] H. Makii,[1,‡] K. Mishima,[1,§] K. Tamura,[2,‖] H. Toyokawa,[3]
H. Ohgaki,[4] J. Golak,[5] R. Skibiński,[5] H. Witała,[5] W. Glöckle,[6] A. Nogga,[7] and H. Kamada[8]

[1]*Research Center for Nuclear Physics, Osaka University, Mihogaoka, Ibaraki, Osaka 567-0047, Japan*
[2]*Department of Physics, Tokyo Institute of Technology, Meguro, Tokyo 152-8551, Japan*
[3]*Research Institute of Instrumentation Frontier, National Institute of Advanced Industrial Science
and Technology, Tsukuba, Ibaraki 305-8568, Japan*
[4]*Institute of Advanced Energy, Kyoto University, Uji, Kyoto 611-0011, Japan*
[5]*M. Smoluchowski Institute of Physics, Jagiellonian University, Krakow, 30-059, Poland*
[6]*Ruhr-Universität, Bochum D-44780, Germany*
[7]*Forschungszentrum Jülich, Institut für Kernphysik (Theorie), D-52425 Jülich, Germany*
[8]*Department of Physics, Faculty of Engineering, Kyushu Institute of Technology,
1-1 Sensuicho, Tobata, Kitakyushu 804-8550, Japan*
(Received 4 October 2005; published 17 March 2006)

A simultaneous measurement of the cross sections of the ³He(γ, p)D and ³He(γ, pp)n reactions has been performed for the first time using monoenergetic pulsed γ-rays at $\langle E_\gamma \rangle = 10.2$ and 16.0 MeV. Charged fragments from the reactions were detected with an efficiency of 100% using a 4π time projection chamber containing ³He gas as an active target. The incident γ-ray flux was measured by a γ-ray detector. Both the track and energy loss signals of charged fragments were obtained in an off-line analysis and used to clearly identify the reaction channel. Thus, the (γ, p) and (γ, pp) cross sections have been determined with small uncertainty. A comparison of the new data to current theory based on the AV18+Urbana IX nuclear forces including π- and ρ-like meson exchange currents shows a severe discrepancy at 10.2 MeV, while at 16.0 MeV data and theory agree within about 12%. Three-nucleon force effects are small, but in general shift the theory in the correct direction.

I. INTRODUCTION

Recent progress in the theoretical analysis of elastic scattering and breakup processes in a three-nucleon system and improving quality of nuclear potentials have provided a promising basis for the studies of the nucleon-nucleon (NN) potential and the role of three-nucleon ($3N$) forces in nuclear reactions [1–3]. Exact theoretical predictions on the three-body reaction processes have been compared to high-precision experimental results to obtain information on the NN and $3N$ forces [4]. Among various reaction studies in the three-nucleon system, an investigation of photodisintegration could play a crucial role because the ground state of the three-nucleon system is well known, the electromagnetic interaction is relatively well known and weak to allow perturbation theory, and photodisintegration in the energy region $E_\gamma < 40$ MeV proceeds mainly via an electric dipole ($E1$) transition [5].

Actually, according to recent rigorous theoretical calculations on the photodisintegration cross sections of the three-body system, these cross sections have been predicted to be sensitive to the NN and $3N$ forces. Two different approaches, the Faddeev method [6] and the hyperspherical harmonic expansion combined with the Lorentz integral transform (LIT) method [7], were employed. The cross sections for the two-body ³He(γ, p)D and three-body ³He(γ, pp)n reactions obtained using the Faddeev method [6] are quite sensitive to the $3N$ forces, especially at energies concentrated around ∼10 and ∼16 MeV. The total cross section obtained using the LIT method [7] also has a similar sensitivity to the NN and $3N$ forces at its peak energy. Note that according to a benchmark calculation of the total ³H photodisintegration cross section performed with these two different approaches using the same NN and $3N$ forces, the calculated cross sections agree quite well with each other [8]. Thus, having the technical performance under control, one is prepared to test the dynamical input, i.e., forces and currents, against data.

Contrary to the significant progress achieved in theoretical calculations, experimental data of the (γ, p) and (γ, pp) cross sections of ³He, which were measured separately using real photons, virtual photons, and/or electrons [9–19], are controversial, as described below.

The (γ, p) cross section was measured by detecting a proton and D with a cloud chamber [9] or with Si detectors [12–15]. The inverse p(D, γ)³He reaction and/or the D(p, γ)³He reaction was also used to obtain the (γ, p) cross section, in which either ³He or a γ-ray was detected by a counter

telescope [16] or a NaI(Tl) detector [11,18]. These measured cross sections agree with each other in the energy region $E_\gamma > 25$ MeV within an experimental uncertainty [13,15]. In the region $E_\gamma < 20$ MeV, however, previous data show a large discrepancy between different data sets, and in the vicinity of the (γ, p) cross section peak they are divided into two discrete groups with a cross section of 0.75 mb [11,15] and of about 1.0 mb [9,12,13]. Note that the latest (γ, p) cross section derived by the (p, γ) reaction is as large as 1.1 mb at $E_\gamma = 10.4$ MeV [18].

The (γ, pp) cross sections were measured mostly by detecting neutrons with BF_3 counters [10,17,19]. The results from different groups show similar excitation functions in the region $E_\gamma < 15$ MeV (except one [10]), but show different structures in the peak region $15 < E_\gamma < 25$ MeV [9,10,17,19]. Note that the data obtained by using the same experimental devices differ from each other, and the origin of the discrepancy was attributed to an incorrect extrapolation of the neutron detector efficiency [19].

In summary, previous (γ, p) and (γ, pp) data are controversial in the region of γ-ray energy $E_\gamma < 20$ MeV and hardly compared to recent theoretical calculations, which show high sensitivity to the NN and $3N$ forces, as described above. The discussion on the (γ, p) data mentioned above, especially the data in the vicinity of the cross-section peak, would suggest that an uncertainty seems to remain in the normalization of these cross sections. Note that previous measurements were made by detecting reaction products at a particular angle with respect to the direction of the incident beams (except one [9]) using different kinds of detectors. Hence, it would be quite difficult to obtain the photodisintegration cross sections of ^{3}He free from systematic uncertainties. Thus, it was necessary to remeasure the cross sections at least at one or two γ-ray energies with the use of a new method to accurately determine the normalization.

Hence, we have performed a new experiment aiming at measuring the (γ, p) and (γ, pp) cross sections simultaneously at the mean reaction energies of $\langle E_\gamma \rangle = 10.2$ and 16.0 MeV with the use of a novel technique combining a pulsed-laser Compton backscattering (LCS) photon beam and a time projection chamber (TPC) [20]. Note that the calculated cross section reaches the peak value, which is sensitive to the $3N$ forces in the vicinity of 10.2 and 16.0 MeV for the (γ, p) and (γ, pp)n reactions, respectively.

The characteristic points of the present experimental method are summarized as follows. First, we used the TPC containing an active ^{3}He gas target, which allowed us to detect all charged low-energy reaction products (fragments) with an efficiency of 100% with a large solid angle of 4π. Note that the kinetic energy of the fragment is quite low from 1 to 7 MeV in the present γ-ray energy region. Second, we could identify the ^{3}He photodisintegration events with a large signal-to-noise ratio, since we obtained the track of a charged fragment from the photodisintegration of ^{3}He in the off-line analysis. Note that the photodisintegration events were produced only during a laser pulse width of 150 ns, and the track of the events should cross the LCS γ-ray beam axis with a small diameter of 2 mm, as described later. Third, we could unambiguously identify an individual photodisintegration reaction channel using the track
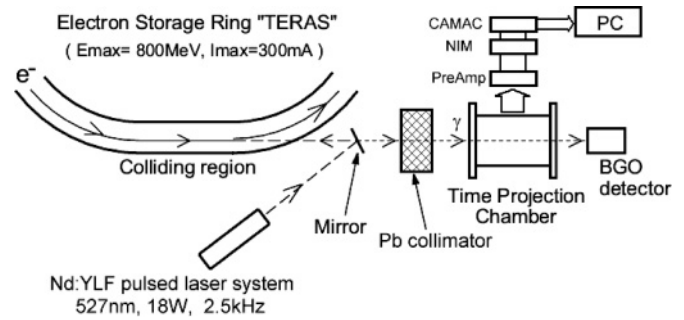

FIG. 1. Schematic view of an experimental setup.

of a charged fragment. Fourth, we could precisely measure the absolute LCS γ-ray flux using a γ-ray detector and determine the ^{3}He-target thickness by measuring the ^{3}He gas pressure and temperature in the TPC. These features could meet the requirements necessary to accurately determine both the ^{3}He(γ, p)D and the ^{3}He(γ, pp)n cross sections with a small systematic uncertainty caused by background, the detection efficiency of the TPC for a charged fragment and an angular distribution effect of charged fragments and so on.

II. EXPERIMENTAL PROCEDURE

The experiment was carried out at the National Institute of Advanced Industrial Science and Technology (AIST) using a pulsed laser-Compton backscattered (LCS) γ-ray beam and a time projection chamber. Beams of LCS γ-rays with maximum energies of $E_\gamma^{max} = 10.5$ and 16.5 MeV were, respectively, obtained by Compton backscattering of pulsed 527 nm Nd-YLF laser lights from 545 and 685 MeV electrons circulating in the electron storage ring TERAS [21]. The pulse width and the repetition rate of the laser light were 150 ns and 2.5 kHz, respectively. A lead collimator was used to obtain monoenergetic LCS γ-rays, and it had a hole with a diameter of 2 mm and a length of 300 mm. The energy spread of the LCS γ-rays was about 4% and its intensity was 10^4 photons/s. The TPC was placed 3 m downstream of the collimator. A schematic view of an experimental setup is shown in Fig. 1.

A. Time projection chamber (TPC)

A detailed description of the TPC is published elsewhere [20]. Hence, we briefly describe the TPC as follows. The TPC was placed inside a 244 mm $\phi \times$ 400 mm vessel, which was filled with a mixed gas of 80% enriched ^{3}He (99.7% enriched in ^{3}He) as a target for the photodisintegration reactions and 20% CH_4 as an operational gas of the TPC. The total pressure was determined to be 1.066 bar at 22.3°C so as to obtain a large pulse height of a charged fragment, which was necessary to easily discriminate a true event from background.

A schematic view of the TPC is shown in Fig. 2. The TPC consists of a drift region with a uniform electric field with an active area of 60×60 mm^2 and a length of 250 mm, and a multiwire proportional counter (MWPC) region with one anode and two cathode planes. The anode plane was sandwiched by the cathode planes with a spacing of 2 mm. The cathode wires in front of and behind the anode plane were stretched along the

NEW DATA FOR TOTAL ^{3}He(γ, p)D and ^{3}He(γ, pp)n ...

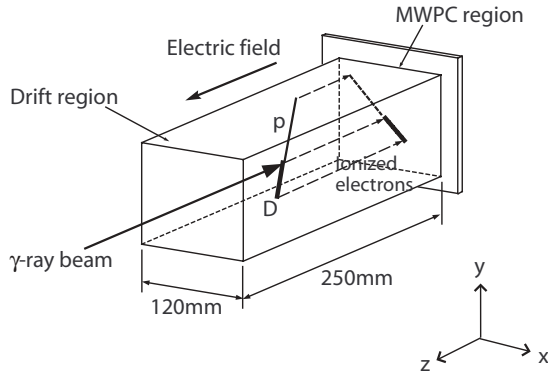PHYSICAL REVIEW C **73**, 034003 (2006)

FIG. 2. Schematic view of a time projection chamber (TPC).

x and y axes to obtain two-dimensional track information of a charged fragment, respectively. The x- and y-directions were defined to be parallel to and perpendicular to the anode wires, respectively. The z-axis was parallel to the LCS γ-ray beam direction.

Two signals of the energy loss and the track of a charged fragment were used to clearly identify the reaction channel. The energy loss rate and path length of a charged fragment from the photodisintegration of ^{3}He and ^{12}C in the TPC were calculated, as listed in Table I. Note that a light fragment, such as a proton or a deuteron, does not stop in the drift region. Anode and cathode signals were produced as follows. First, secondary electrons were produced along the path of a charged fragment. The electrons were drifted along a uniform electric field to the MWPC region and multiplied via an avalanche process. The avalanche signals were picked up by the anode and cathode wires, respectively. Using the signals from the cathode wire we constructed the trajectory of a charged fragment on the x-y plane. We determined the z-position of a charged fragment by measuring the drift time, T_D, of electrons, which was given as $T_D = T_1 - T_0$. Here, electrons were produced at a time T_0, and the avalanche process occurred at a time T_1. The anode signal was used to obtain the energy loss rate of a charged fragment in the drift region.

Here, it should be mentioned about a decrease in an anode pulse height arising from electronegative pollutants such as oxygen, which could be contained in the TPC gas [22]. We purified the mixed gas using a high purity filter to operate the TPC with little problem. The performance of the TPC was studied using the α-ray source of ^{241}Am and a Si detector. The energy resolution of the TPC and the drift velocity of ionized electrons were measured as being 7.5% at FWHM per unit anode wire and 10.2 ± 0.2 mm/μs, respectively. The position resolution along the z-direction was obtained as being 0.33 mm. The spatial resolution was 2 mm for both the x-coordinate and the y-coordinate, respectively, since each wire on the anode and cathode planes was stretched with a spacing of 2 mm.

B. Data acquisition system

The data acquisition system is described below. Signals from cathode wires were used to obtain stop signals for a time-to-digital converter (TDC). A common start signal for the TDC was obtained from the output of a pulsed laser clock. The TDC was used to record both the times of the leading edge and the trailing edge for one anode signal. The time difference between these two edges provided information about the amount of energy loss of a charged fragment in the drift region, as described later. In order to measure the amount of energy loss by integrating the current of an anode signal, we recorded the anode signal shape using a flash analog-to-digital converter (FADC) and constructed a charge-integrated spectrum of a charged fragment in an off-line analysis. Note that the anode signal was obtained by summing signals from several anode wires on either the right-hand side or the left-hand side with respect to the z-axis. Data from CAMAC modules were acquired by a personal computer and recorded on a hard disk drive in a list mode. The count rate of the TPC was quite low, $\sim$1 cps at $E_\gamma^{\max} = 10.5$ MeV and $\sim$0.5 cps at 16.5 MeV, respectively. Hence, the dead time of the system was less than a few % during experimental runs and the photodisintegration cross sections of ^{3}He were obtained by correcting for the dead time.

III. DATA ANALYSIS AND RESULTS

A. Event identification

We observed photodisintegration events of ^{3}He and ^{12}C from CH$_4$ gas, and electron background and natural background. Note that the total event rate was a few counts per

TABLE I. Energy loss rate ΔE (in units of keV/30 mm) and path length l_p (in units of mm) of a fragment from the photodisintegrations of ^{3}He and ^{12}C in the TPC.

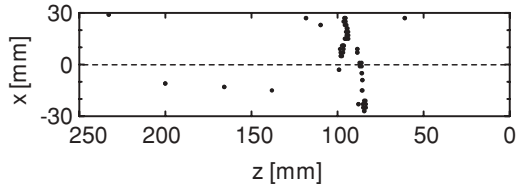| Reaction | Q | Fragment | $E_\gamma^{\max}$ | | | |
| | | | 10.5 MeV | | 16.5 MeV | |
	(MeV)		ΔE	l_p	ΔE	l_p
^{3}He(γ, p)D	-5.493	p	105	545	55	2245
		d	321	103	169	386
^{3}He(γ, pp)n	-7.718	p	$0 \sim 594$	$0 \sim 198$	$0 \sim 591$	$0 \sim 1494$
^{12}C$(\gamma, p)^{11}$B	-15.957	p			498	23
		^{11}B			45	1

FIG. 3. Typical track of electron background.

second, and the photodisintegration event rate was about 0.5% of the background. In order to pick-up the photodisintegration events, we first identified background events, as described below.

1. Background events

There were electron background and natural background, as described below.

(1) Electron background. Electron background was produced by the interaction of the LCS γ-rays with atomic electrons of ^{3}He and CH_4. Since the electron energy was in the range from a few mega electron volts to tens of mega electron volts, the electron energy loss rate in the TPC was quite small, on the order of 0.1 keV/mm. Hence, most of the electron background could be discriminated by the discriminator for the cathode wire. Only some electrons, which could exceed the discriminator, were observed, as shown in Fig. 3. Here, we could easily identify electron background events by their small pulse height and also by the facts that electron background produced neither secondary electron clouds nor crossed the LCS photon beam axis, as clearly shown in Fig. 3.

(2) Natural background. A natural background event was easily identified, since it was not correlated with the pulsed LCS γ-rays beam and its track did not cross the beam axis, as shown in Fig. 4. Hence, we could clearly discriminate the background from the photodisintegration events of ^{3}He and ^{12}C. This natural background might be because of an α-particle from natural radioactivity, such as radon contained in the TPC chamber or in the mixed gas of enriched ^{3}He and CH_4, since the pulse height of the natural background was much higher than that of electrons. Other background, such as cosmic muons, and β- and γ-rays from the decay of natural radioactivity (^{40}K and/or ^{208}Tl), was not the main background, since most of them could be discriminated by the discriminator because of their little energy deposit in the TPC.

2. Photodisintegration events of ^{3}He and ^{12}C

Since both electron and natural background events were identified as described above, background-free (BF) events
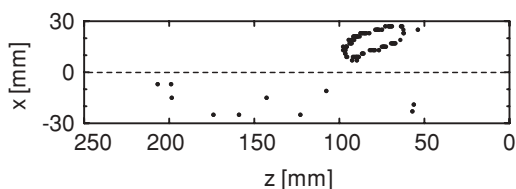

FIG. 4. Typical track of natural background.

could be picked up from all events recorded on the FADC. The BF events contained the photodisintegration events of ^{3}He and ^{12}C. At this point, it should be mentioned about the two- and three-body photodisintegrations of ^{12}C. Since the Q-values for the ^{12}C(γ,n)^{11}C and ^{12}C(γ, p)^{11}B reactions are -18.72 and -15.96 MeV, respectively, and that for the ^{12}C(γ, $\alpha\alpha$)^{4}He reaction is -7.37 MeV, the latter reaction events could be observed at $E_\gamma^{max} = 10.5$ and 16.5 MeV and the ^{12}C(γ, p)^{11}B ones could be observed only at 16.5 MeV.

We assigned a reaction channel of the BF events by referring to the path length, the pulse height and the track width as well as the reaction kinematics of each BF event. Since the path length of a charged fragment from the ^{3}He photodisintegration significantly differs from that of ^{12}C, as listed in Table I, we used it to unambiguously assign the reaction channel of a charged fragment together with the pulse height spectrum and the track width. The measured pulse height spectrum of a charged fragment was compared to the calculated one by a Monte Carlo method, as described later. The track width was obtained by converting both the times of the leading edge and the trailing edge of a cathode signal into the z-coordinate of the fragment track. The track width could provide information about the energy loss of a charged fragment, since the time difference between these two edges is larger with increasing pulse height of a cathode signal, and thus its track width becomes wider. Hence, the track width of a charged fragment was useful to assign the reaction channel of the fragment.

(1) Two-body channels of ^{3}He and ^{12}C photodisintegrations. Two fragments of a proton and a deuteron (or a proton and ^{11}B) from the two-body channel of ^{3}He (or ^{12}C) are emitted in opposite directions with respect to the LCS γ-ray beam direction with equal momentum in the center-of-mass system.

(i) ^{3}He(γ, p)D channel

A typical track of two fragments of a proton and a deuteron obtained at $E_\gamma^{max} = 16.5$ MeV is shown in Fig. 5. Since both path lengths of two fragments are longer than $\sim$1 mm, the observed event can be assigned as being the ^{3}He(γ, p)D reaction event, but not the ^{12}C(γ, p)^{11}B reaction one.

Based on the argument described above, we assigned a deuteron for an event wider in the track width. The sum spectrum of the measured pulse height of a proton and a deuteron agrees nicely with the calculated one, as shown in Fig. 6(a), within the statistical uncertainty. The calculation was made while assuming that the fragments were from the ^{3}He(γ, p)D reaction channel. Similarly to the case mentioned above, a typical sum spectrum of the measured pulse height

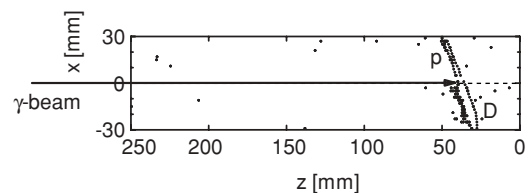FIG. 5. Example of the tracks of the charged fragments from ^{3}He(γ, p)D reaction (side view). The dots indicate the envelopes of the electron clouds produced by the fragments.
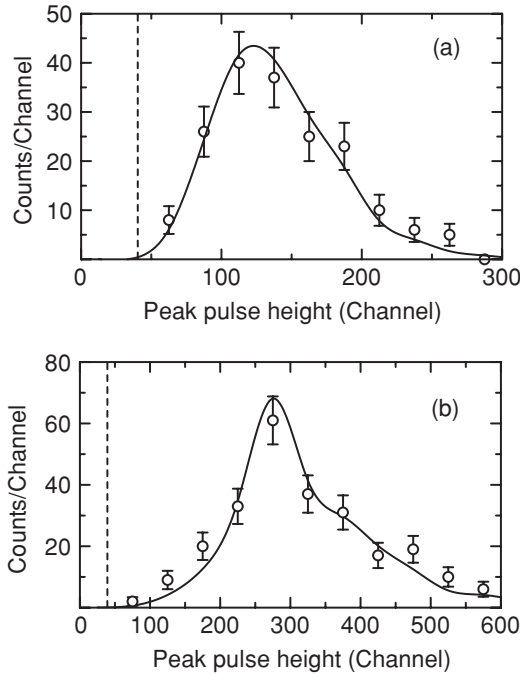
FIG. 6. Total pulse height spectrum from the ^{3}He(γ, p)D reaction at $E_\gamma^{\max} = 16.5$ MeV (a) and 10.5 MeV (b), respectively. The solid curves are the spectra calculated by a Monte Carlo method.

of a proton and a deuteron taken at $E_\gamma^{\max} = 10.5$ MeV agrees with the calculated one, as shown in Fig. 6(b).

(ii) ^{12}C(γ, p)^{11}B channel

An event of this channel can be clearly separated from that of the ^{3}He(γ, p)D reaction channel, since the path length of a proton and ^{11}B is much shorter than that of a proton and a deuteron from the latter channel. We did not observe any candidate event of this channel in the present experimental statistics.

(1) Three-body channels of ^{3}He and ^{12}C photodisinte-grations. Fragments tracks from the three-body channels of ^{3}He and ^{12}C are randomly oriented with respect to one another and with respect to the LCS γ-ray beam axis in the center-of-mass system. This feature is quite different from that of the two-body channel. Events from the ^{3}He(γ, pp)n reaction can be unambiguously discriminated from the ^{12}C(γ, $\alpha\alpha$)^{4}He reaction, since the former reaction provides two tracks and the latter gives three tracks.

(i) ^{3}He(γ, pp)n channel

In Fig. 7 we show the tracks of charged fragments from this channel obtained at $E_\gamma^{\max} = 16.5$ MeV. The tracks of two protons cross the LCS γ-ray beam axis and are randomly oriented with respect to each other and with respect to the LCS γ-ray beam direction.

The sum spectrum of the observed pulse height of these charged fragments is in good agreement with the calculated one, as shown in Fig. 8(a). The calculation was made while assuming that the charged fragments were from the ^{3}He(γ, pp)n reaction. Here, the second peak reflected to the energy spectrum of the proton used in the calculation [23].
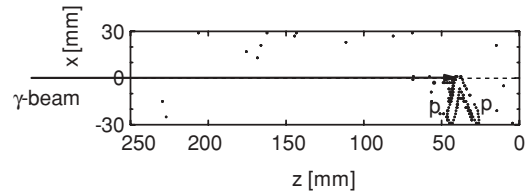

FIG. 7. Example of the tracks of the charged fragments from ^{3}He(γ, pp)n reaction (side view).

Similarly to the case mentioned above, a typical sum spectrum obtained at $E_\gamma^{\max} = 10.5$ MeV agrees with the calculated one, as shown in Fig. 8(b). Here it should be mentioned about the track of a charged fragment from the three-body channel, which could resemble a charged fragment from the two-body channel in the track. Namely, two protons from the two-body channel could be emitted in the opposite direction and/or in the same direction with respect to each other and with respect to the LCS γ-ray beam direction. In the former case, the neutron is emitted in the same direction as one of the two protons, and in the latter case the neutron is emitted in the opposite direction with respect to the two protons direction. We observed two events corresponding to the former case, and did not observe any candidate event corresponding to the latter case. We assigned these two events to the three-body channel based on their same narrow track width compared to that of a deuteron.

(ii) ^{12}C(γ, $\alpha\alpha$)^{4}He channel

Three tracks of particles, which are randomly oriented with respect to one another and with respect to the LCS γ-ray beam direction in the center-of-mass system, were observed,
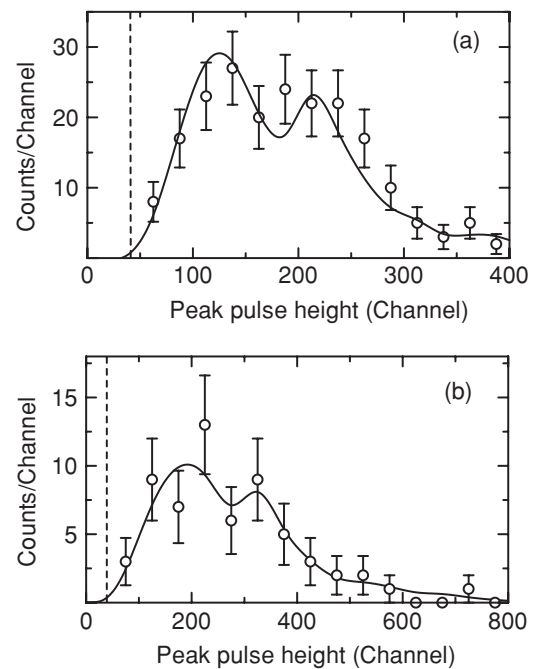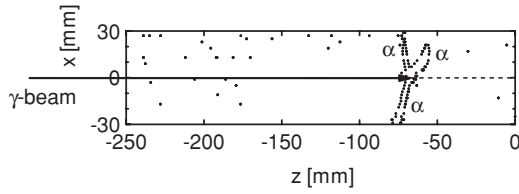

FIG. 8. Total pulse height spectrum from the ^{3}He(γ, pp)n reaction at $E_\gamma^{\max} = 16.5$ MeV (a) and 10.5 MeV (b), respectively. The solid curves are the spectra calculated by a Monte Carlo method.

FIG. 9. Typical track of the ^{12}C$(\gamma, \alpha\alpha)\alpha$ event.

as shown in Fig. 9. All of the track width is similarly wide. Hence, we could clearly assign this event as the ^{12}C$(\gamma, \alpha\alpha)^4$He channel.

B. Cross sections of the photodisintegration of ^{3}He

A partial cross section $\sigma_i(E\gamma)$ corresponding to the two-body and/or the three-body photodisintegration of ^{3}He at the γ-ray energy E_γ is given by taking into account both the finite energy spread of the incident LCS γ-rays and the γ-ray energy dependence of the TPC efficiency, as follows [24]:

$$Y_i = N_t \cdot L \cdot \Phi \times \frac{\int_0^{E_\gamma^{\max}} \varepsilon_i(E_\gamma) \cdot \sigma_i(E_\gamma) \cdot \phi(E_\gamma) dE_\gamma}{\int_0^{E_\gamma^{\max}} \phi(E_\gamma) dE_\gamma}. \quad (1)$$

Here, Y_i, N_t, L and Φ stand for the yield of a reaction channel, the number density of the target nuclei, the effective length of the TPC, and the incident LCS γ-ray flux, respectively. The parameter $\phi(E_\gamma)$ denotes the incident LCS γ-ray intensity at the energy E_γ. $E_\gamma^{\max}$ denotes the maximum energy of the LCS γ-ray. The parameter $\varepsilon_i(E_\gamma)$ is the energy dependent detection efficiency of the TPC for a charged fragment. The average cross section, $\langle\sigma_i\rangle$, and the weighted-mean reaction energy, $\langle E_\gamma\rangle$, are, respectively, defined as follows:

$$\langle\sigma_i\rangle = \frac{\int_0^{E_\gamma^{\max}} \varepsilon_i(E_\gamma) \cdot \sigma_i(E_\gamma) \cdot \phi(E_\gamma) dE_\gamma}{\int_0^{E_\gamma^{\max}} \varepsilon_i(E_\gamma) \cdot \phi(E_\gamma) dE_\gamma}$$

$$= \frac{Y_i}{N_t \cdot L \cdot \int_0^{E_\gamma^{\max}} \varepsilon_i(E_\gamma) \cdot \phi(E_\gamma) dE_\gamma}, \quad (2)$$

$$\langle E_\gamma\rangle_i = \frac{\int_0^{E_\gamma^{\max}} E_\gamma \cdot \varepsilon_i(E_\gamma) \cdot \sigma_i(E_\gamma) \cdot \phi(E_\gamma) dE_\gamma}{\int_0^{E_\gamma^{\max}} \varepsilon_i(E_\gamma) \cdot \sigma_i(E_\gamma) \cdot \phi(E_\gamma) dE_\gamma}. \quad (3)$$

The parameters ε_i, N_t, L, Φ and ϕ were determined as described in the next subsections.

1. Detection efficiency, $\varepsilon_i(E_\gamma)$, and effective length, L

The signal of secondary electrons was picked up by both the anode and the cathode wires. Hence, the TPC efficiency, $\varepsilon_i(E_\gamma)$, is expected to be 100% along the whole drift length of 250 mm. Although the efficiency was not constant in the whole drift length of 250 mm because of the distortion of the electric field strength at both the edges of $z = 0$ and 250 mm, it was found to be more than 99.5% in the region of between $z = 12.5$ and 237.5 mm by measuring the pulse height spectrum of an α-particle from the decay of ^{241}Am along the z-direction in the drift space [20].

In the present study an effective length L was defined as 180 mm in the region between $z = 25$ and 205 mm so that

a charged fragment track could be clearly observed by taking into account of the z-position resolution of 2 mm. Note that the path length of a proton and a deuteron from the two- and three-body decays of ^{3}He is longer than that of the α-ray.

It should be mentioned that the levels of discriminators used to reject the electric noise of both the anode and the cathode signals and the electron background were set as low as possible. In order to further reduce the events due to electron background, we set the software threshold level higher than those of the discriminators. Hence, it is necessary to quantitatively determine the TPC efficiency by investigating a possible change of the efficiency because of the threshold level. An investigation was carried out by comparing the measured pulse peak spectrum of a charged fragment to the calculated one, as described below. A pulse peak height was obtained as the maximum peak height of an instantaneous waveform of an anode pulse recorded by FADC. A calculated spectrum was obtained using a Monte Carlo code, which simulated the kinematics of the photodisintegration events, the migration of drift electrons, and the pulse shapes of the signals from the anode and cathode wires [24].

We made the Monte Carlo code as follows. First, a photodisintegration reaction point induced by LCS γ-rays of given energy was chosen at random on the γ-rays beam z-axis. Here, the LCS γ-ray energy spectrum was measured with an NaI(Tl) detector, as described later. Second, a fragment track from a photodisintegration reaction of ^{3}He was calculated by considering the LCS γ-ray energy and a Q-value of a photodisintegration reaction. In order to calculate the emission angle of a charged fragment, we used experimental results, which were the $E1$ distribution for the two-body channel [25] and an isotropic one for the three-body channel, respectively. We used a theoretical value for the energy distribution of a proton or a neutron from the three-body channel [23], since the value agrees with a measured one [9]. Third, the energy deposited by a charged fragment was calculated as a function of the distance from a reaction point to a certain point in the TPC drift region using the energy loss formula given by Ziegler [26]. The thus-obtained energy was converted to the number of ionized electrons using the ionization energy of electrons in the TPC gas. Fourth, the drift time of ionized electrons was calculated using the measured drift velocity [20]. Consequently, calculated event data of FADC and TDC were obtained for each wire using the drift time, the shaping time of an amplifier and the threshold level of a discriminator. The event data were recorded and analyzed with the same procedure as for the data of the real measurements to determine the TPC efficiency.

The efficiencies $\varepsilon(\gamma, p)$ and $\varepsilon(\gamma, pp)$ for the two-body and three-body channels were respectively obtained by taking the ratio of number of events above a discrimination level for anode signals to all events above a zero level for each channel, as given below:

$$\varepsilon(\gamma, p) = \frac{Y_i(\gamma, p)_{\mathrm{discri.}=\Delta}}{Y_i(\gamma, p)_{\mathrm{discri.}=0}}, \quad (4)$$

$$\varepsilon(\gamma, pp) = \frac{Y_i(\gamma, pp)_{\mathrm{discri.}=\Delta}}{Y_i(\gamma, pp)_{\mathrm{discri.}=0}}. \quad (5)$$

Here, $Y_i(\gamma, p)_{\text{discri.}=\Delta}$ and $Y_i(\gamma, p)_{\text{discri.}=0}$, and $Y_i(\gamma, pp)_{\text{discri.}=\Delta}$ and $Y_i(\gamma, pp)_{\text{discri.}=0}$ are the yield for the two-body and three-body channels taken by FADC with the discrimination level, Δ, and that with the level $\Delta = 0$, respectively. They were obtained by integrating a calculated pulse height spectrum $\{PH\}_{\text{cal.}}$ in the region above $\{PH(\gamma, p)\}_{\text{cal.}} \geqslant \Delta$, and $\{PH(\gamma, pp)\}_{\text{cal.}} \geqslant \Delta$, respectively. The calculated spectra $\{PH(\gamma, p)\}_{\text{cal.}}$ and $\{PH(\gamma, pp)\}_{\text{cal.}}$ are compared to the observed ones in Figs. 6 and 8, respectively. Here, we can clearly see that the calculated spectra for $E_\gamma^{\max} = 10.5$ and 16.5 MeV agree nicely with the observed ones. In addition, the pulse heights for the observed (γ, p) and (γ, pp) events were found to be well above the discrimination level, Δ. Hence, $Y_i(\gamma, p)_{\text{discri.}=\Delta}$ and $Y_i(\gamma, pp)_{\text{discri.}=\Delta}$ agree quite well with $Y_i(\gamma, p)_{\text{discri.}=0}$ and $Y_i(\gamma, pp)_{\text{discri.}=0}$, respectively, and thus the TPC efficiencies, $\varepsilon(\gamma, p)$ and $\varepsilon(\gamma, pp)$, are considered to be 100%.

Here, it should be mentioned about the decrease in the pulse height of a charged fragment during the drift process of secondary electrons to the anode plane in the TPC. It is well known that if the TPC contains electronegative pollutants, such as oxygen and water, these pollutants could capture a certain amount of electrons during the drift process [22], and the pulse height of a charged fragment would be lower with increasing the drift length of electrons. If this decrease in the peak height would occur, one has to correct for the decrease to compare the measured pulse height spectrum of a charged fragment to the calculated one. Since the mixed gas of ^{3}He and CH_4 was found to contain 0.007% H_2O and 0.3% oxygen by the mass analysis of the mixed gas, we purified the TPC gas using a high purity filter. The pulse height of a charged fragment, however, was found to decrease slightly with increasing the drift length of electrons. Hence, we corrected for the amount of the decrease in the Monte Carlo calculation mentioned using a correction factor, which was obtained experimentally using the deuteron data from the ^{3}He(γ, p)D reaction.

The pulse peak height of a charged fragment calculated in the range from $z = 25$ to 205 mm agrees with the corrected peak spectrum both for the (γ, p) and (γ, pp)n channels, as mentioned above. An admixture of higher multipole transitions does not affect the data analysis significantly, since the ^{3}He photodisintegration events have been detected with a geometry of 4π by the TPC.

2. Target number density, N_t

The ^{3}He target density, N_t, was obtained by measuring the mixed gas pressure of ^{3}He and CH_4 and its temperature in the TPC, as follows:

$$N_t = \frac{p \cdot P \cdot N_A}{R \cdot T}. \qquad (6)$$

Here, p, P, N_A, R, and T are the partial pressure of ^{3}He, the total gas pressure, Avogadro's number, the gas constant, and the temperature, respectively. The total pressure and the temperature were kept constant with a slight fluctuation of 0.4% during the measurements. The number, N_t, for the measurements at $E_\gamma^{\max} = 10.5$ and 16.5 MeV was derived to be 2.08×10^{19} and 2.06×10^{19} atoms/cm^3, respectively.
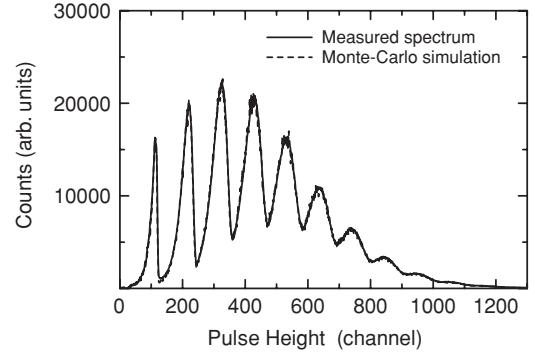

FIG. 10. Typical γ-ray pulse height spectrum measured at $E_\gamma^{\max} = 10.5$ MeV with a BGO detector. The average γ-ray yield per pulse, M, was determined to be 4.48 by fitting the spectrum.

3. Incident photon flux, Φ

The incident LCS γ-ray spectrum was measured to determine its flux, Φ, by using a BGO detector with a diameter of 50.8 mm and a length of 152.4 mm. A typical measured γ-ray spectrum is shown in Fig. 10, in which we see multiple peaks because of pile-up effects of the LCS γ-rays, as described below.

Both the laser photon beam and the electron beam were pulsed with a width of 150 ns and 6 ns, and with a repetition rate of 2.5 kHz and 100 MHz, respectively. Hence, one laser pulse could make several collisions with the bunched electron beam within the one laser pulse, and thus generate multiple LCS γ-ray peaks as being pile-up effects of the LCS γ-rays. Note that the time difference between the multiple peaks was so short that these peaks were hardly decomposed into an individual LCS γ-ray.

The photodisintegration yield of ^{3}He is proportional to an averaged number, M, of multiple LCS γ-rays per laser pulse. The number M was obtained by comparing a measured BGO spectrum to a calculated one obtained by a Monte Carlo method [27]. The Monte Carlo calculation was made considering the production procedure of multiple peaks as follows. First, the LCS γ-ray yield is proportional to the number of electrons times that of laser photons. The probability density for generating LCS γ-rays per laser pulse is so small that the LCS γ-ray yield would follow a Poisson distribution. Second, the electron beam in the TERAS can be assumed to be a continuous beam because its repetition rate is much higher than that of the laser photon beam. Third, the observed multiple peaks of the LCS γ-ray spectrum are assumed to be the sum of the pulse height spectrum of each LCS γ-ray, since the BGO detector responds to each γ-ray independently. The response function of the BGO detector to one LCS γ-ray photon was obtained by measuring the γ-ray spectrum with low flux, which was free from multiple peaks. Fourth, the pulse shape of the BGO detector for multiple LCS γ-rays was obtained using both the time distribution of the LCS γ-ray measured by a plastic scintillation counter and a shaping time of 1 μs of an amplifier used for the BGO detector. The response function of the BGO detector with an averaged number M of multiple LCS γ-rays was calculated by a Monte-Carlo method, and the number M was obtained by fitting a measured spectrum

with the multiple peaks with the calculated response function. A typical measured spectrum is in good agreement with the calculated one with $M = 4.48 \pm 0.09$, as shown in Fig. 10. Using the resultant number M, the LCS γ-ray total flux Φ was obtained as follows:

$$\Phi = M \times f \times T_L. \tag{7}$$

Here, f is the frequency of the laser pulse, and T_L is the live time of measurement system of the TPC. The γ-ray flux was obtained with an error of about 2%, which consisted of statistics of the LCS γ-ray yield, and uncertainties of the response function of the BGO detector as well as the least-square fitting for the LCS γ-ray spectrum with multiple peaks measured with the BGO detector. Note that if we used an incomplete response function of the BGO detector, we failed to reproduce the linearity of the measured spectrum with multiple peaks. The averaged number M was found to decrease with decreasing the number of electrons. Since we took the data of the ^{3}He photodisintegration in an event-by-event mode, and during the data taking period we also measured the LCS γ-ray spectrum using the BGO detector, we could obtain the value of M accurately.

4. Energy spectrum of incident LCS γ-ray $\phi(E_\gamma)$

The LCS γ-ray spectrum has a finite energy spread because of the finite width of the lead collimator and of the emittance of electron beams of the TERAS. It is, therefore, necessary to measure the intrinsic energy spectrum, $\phi(E_\gamma)$, of the incident LCS γ-rays to determine the weighted-mean energy of the photodisintegration reaction of ^{3}He. The spectrum was measured using an anti-Compton NaI(Tl) spectrometer, which comprised a central NaI(Tl) detector with a diameter of 76.2 mm and a length of 152.4 mm, and an annular one with an outer diameter of 254 mm and a length of 280 mm. A typical spectrum measured at $E_{\max} = 16.5$ MeV is shown in Fig. 11. Using a response function of the NaI(Tl) detector calculated by a simulation code [28], the intrinsic energy spectrum of the LCS γ-ray was obtained as shown in Fig. 11. The energy resolution (FWHM) of the LCS γ-rays was determined to be 0.350 MeV at $E_\gamma^{\max} = 10.5$ and 0.86 MeV at 16.5 MeV with an uncertainty of 10%, respectively. Here, it should be mentioned that the γ-ray energy spectrum taken with the NaI(Tl) spectrometer using γ-ray sources, such as
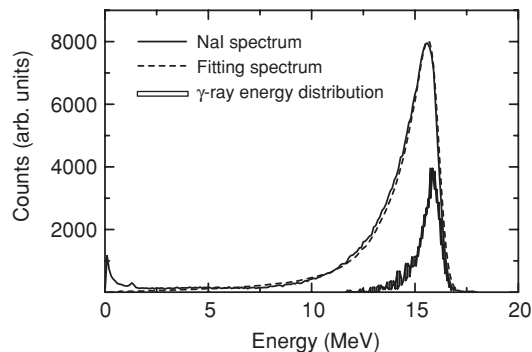
FIG. 11. Typical incident LCS γ-ray spectrum measured at $E_\gamma^{\max} = 16.5$ MeV with a NaI(Tl) detector.

TABLE II. Total ^{3}He photodisintegration cross sections (in units of mb) at 10.2 and 16.0 MeV. $\sigma(\gamma, p)$ refers to the pd channel, $\sigma(\gamma, pp)$ to the 3N breakup channel and $\sigma(\gamma, p) + \sigma(\gamma, pp)$ is the sum of both.

	$\langle E_\gamma \rangle$ (MeV)	AV18	AV18+Urbana IX	Exp.
$\sigma(\gamma, p)$	10.2	1.01	0.96	0.77(5)
$\sigma(\gamma, p)$	16.0	0.71	0.72	0.65(5)
$\sigma(\gamma, pp)$	10.2	0.55	0.49	0.15(5)
$\sigma(\gamma, pp)$	16.0	1.07	1.04	0.91(6)
$\sigma(\gamma, p)/\sigma(\gamma, pp)$	10.2	1.84	1.96	5.1(16)
$\sigma(\gamma, p)/\sigma(\gamma, pp)$	16.0	0.67	0.69	0.71(4)
$\sigma(\gamma, p) + \sigma(\gamma, pp)$	10.2	1.56	1.45	0.92(8)
$\sigma(\gamma, p) + \sigma(\gamma, pp)$	16.0	1.78	1.76	1.56(9)

^{22}Na, ^{88}Y, and ^{137}Cs, and the 7.65 MeV γ-ray from the ^{56}Fe$(n, \gamma)^{57}$Fe reaction was shown to be in good agreement with the calculated one using the simulation code mentioned above [28].

5. Photodisintegration cross section of ^{3}He

The two-body, three-body, and total photodisintegration cross sections of ^{3}He were determined using the values of $Y_i, \varepsilon_i, N_t, L, \phi(E_\gamma)$, and Φ, as given in Table II; they are shown together with previous ones in Figs. 12(a), 12(b), and 12(c), respectively.
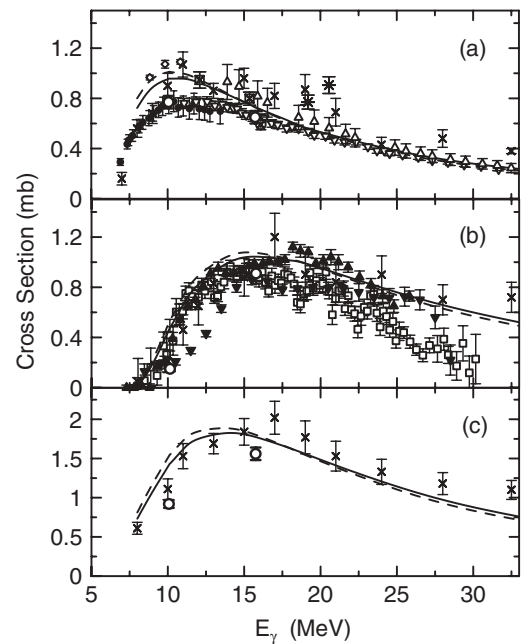
FIG. 12. ^{3}He photodisintegration cross section: (a) ^{3}He(γ, p)D, (b) ^{3}He(γ, pp)n, and (c) total photoabsorption. Present (open circles), Ref. [9] (crosses), Ref. [10] (filled downward triangles), Ref. [11] (filled circles), Ref. [12] (crossed squares), Ref. [13] (open upward triangles), Ref. [14] (asterisks), Ref. [15] (open downward triangles), Ref. [16] (crossed circles), Ref. [17] (open squares), Ref. [18] (diamonds), Ref. [19] (filled upward triangles). The solid curves and the dashed ones indicate the calculated cross sections using the inter-nucleon potentials of the AV18+Urbana IX and the AV18 alone, respectively.

Here, the quoted uncertainty is the result of the combined uncertainties on the statistics of the reaction yield, and a systematic uncertainty of about 3%, 2% from the incident γ-ray flux, 1% from the target number of ^{3}He, and less than 1% from the effective length of the TPC.

The present ^{3}He(γ, p)D data agree with the data sets with a lower cross section of 0.75 mb [11,15], contrary to the larger value of 1.0 mb [9,12,13] and the latest value of 1.1 mb derived from the (p, γ) reaction [18].

Concerning the ^{3}He(γ, pp)n channel, the present datum agrees with all previous data at $\langle E_\gamma \rangle = 16.0$ MeV [9,10,17,19], and with that at 10.2 MeV [10] within the experimental uncertainty. However, the present data deviates from other two data at 10.2 MeV [17,19], which were obtained by detecting the neutrons. Note that in these two experiments true neutrons events were obtained by subtracting the background neutrons produced by photodisintegration reactions by various materials placed in an experimental room. Hence, one might have a problem to discriminate the true neutrons events from the background, especially when the cross section is very low in the threshold energy region, such as 10.2 MeV. On the contrary, the present datum was obtained by detecting a charged fragment from the ^{3}He(γ, pp)n reaction with the TPC, but not a neutron; therefore, any charged fragment could be detected with 100% efficiency, being free from the uncertainty of the efficiency inherent to a neutron detector, as described before.

The present (γ, p) and (γ, pp) data are about 20% $\sim$ 30% smaller than those of the old simultaneous measurement [9]. One of the main reasons of the discrepancy could be due to normalization of the incident γ-ray flux. The normalization was made by two different methods, e.g., with use of a quanta-meter and of the integrated cross section of 0.032 $\pm$ 0.003 MeV·b [29] for the ^{12}C$(\gamma, n)^{11}$C reaction; the obtained cross sections agreed with each other within an uncertainty of 3% [29]. The integrated cross section, however, was revised to be 0.023 $\pm$ 0.001 MeV·b [30], and therefore the reported data [9] should be reduced by 28%. The thus-renormalized cross sections should be noted to be in good agreement with the present data for both the ^{3}He(γ, p)D and ^{3}He(γ, pp)n channels.

IV. COMPARISON TO THEORY

The present (γ, p), (γ, pp), and total $\{(\gamma, p)+(\gamma, pp)\}$ data are compared to our calculations in Table II and Figs. 12a, 12b, and 12c. The theoretical total cross sections were obtained using exact solutions of the three-body Faddeev equations for the ^{3}He target state and for the two-body p-d or three nucleon outgoing scattering states. These states were calculated consistently either with the nuclear Hamiltonian based on the AV18 potential [31] only or combined with the Urbana IX $3N$ force [32]. For the ^{3}He state, we also included electromagnetic interactions, but not for the $3N$ continuum. For the current operator of the three nucleon system, the standard nonrelativistic single nucleon piece and the two-body currents of the π- and ρ-exchange type related to the AV18 force, as proposed by Riska [33], have been used [34,35].

We can see, in Figs. 12a–c that in all cases the $3N$ force effects are rather small (around 5%, except at $\langle E_\gamma \rangle =$ 10.2 MeV in the three nucleon breakup, where they reach 12%). Now, comparing to the new data at 10.2 MeV, we overshoot the pd results by 24%. The situation for the $3N$ breakup is even worse. Here, our predictions miss the data by a factor of 3. However, we note that the $3N$ forces move the predictions in the correct direction. One might think that a part of that discrepancy is caused by the Coulomb force, which is neglected in the continuum. However, a recent work [36] shows that this discrepancy can not be fully explained by the lack of the Coulomb force in our theoretical framework. As a matter of fact, the Coulomb force at photon energy of 10 MeV decreases the pd and $3N$ cross sections by about 10% and 25%, respectively [37]. The situation at 16.0 MeV is much more favorable, comparing the theory and the data. In the pd channel, the theory overshoots the data by about 10% and in the $3N$ break up by about 14%. The serious discrepancy at 10.2 MeV in the $3N$ breakup is also reflected in the total ^{3}He breakup cross section and to a much lesser extent at 16.0 MeV. Since the $3N$ force effects decrease the total cross sections in both channels at 10.2 MeV, one might form the ratio $\sigma(\gamma, p)/\sigma(\gamma, pp)$ and compare it without and with the $3N$ forces. This ratio might be less dependent on the $3N$ forces. This is indeed the case, as Table II shows. The theoretical value at 10.2 MeV of about 2, however, deviates dramatically from the experimental value of about 5.

V. CONCLUSION

It is the first time that the simultaneous measurement of the (γ, p) and (γ, pp) reaction cross sections of ^{3}He has been performed using monoenergetic pulsed laser Compton backscattered γ-rays and a time projection chamber containing ^{3}He gas as an active target at the mean reaction energies of $\langle E_\gamma \rangle = 10.2$ and 16.0 MeV, peak energies of the (γ, p) and (γ, pp) reaction cross sections sensitive to NN and $3N$ forces, respectively. The new experimental method employed allowed us to detect a reaction product with high detection efficiency of 100% with the 4π geometry, which is essential to accurately determine the cross sections with small uncertainty.

In conclusion, the nuclear force model AV18+Urbana IX, which gives a fairly good description of the bound-state energies in light nuclei, and a rather good description of low-energy $3N$ scattering observables; together with a choice of two-body currents of the π- and ρ- like nature have been applied to an evaluation of the total (γ, p) and (γ, pp) cross sections at $\langle E_\gamma \rangle = 10.2$ and 16.0 MeV. The agreement with the data at 16.0 MeV is reasonably good (about 10%–14% above the data), but there is in strong disagreement at 10.2 MeV, especially in the $3N$ breakup channel. From the experimental side it is important to measure with high precision the (γ, p) and (γ, pp) cross sections from the threshold region up to the respective peak cross sections for a larger number of incident photon energies. Independently, it will be very interesting to apply the more basic and systematic approach based on effective field theory constrained by chiral symmetry to those low-energy observables. Very promising work in the pure $3N$ sector has already appeared [2] and is going on [38], and consistent coupling of the photon in that framework is under consideration.

[1] C. R. Chen, G. L. Payne, J. L. Friar, and B. F. Gibson, Phys. Rev. C **33**, 1740 (1986); P. Sauer, Prog. Part. Nucl. Phys. **16**, 35 (1986); Y. Wu, S. Ishikawa, and T. Sasakawa, Few-Body Syst. **15**, 145 (1993); W. Glöckle, H. Witała, D. Huber, H. Kamada, and J. Golak, Phys. Rep. **274**, 107 (1996); A. Nogga, H. Kamada, and W. Glöckle, Phys. Rev. Lett. **85**, 944 (2000); M. Viviani, Nucl. Phys. **A631**, 111c (1998); J. Carlson and R. Schiavilla, Rev. Mod. Phys. **70**, 743 (1998).

[2] E. Epelbaum, A. Nogga, W. Glöckle, H. Kamada, Ulf-G. Meißner, and H. Witała, Phys. Rev. C **66**, 064001 (2002).

[3] J.-I. Fujita and H. Miyazawa, Prog. Theor. Phys. **17**, 360 (1957); S. A. Coon, M. D. Scadron, P. C. McNamee, B. R. Barrett, D. W. E. Blatt, and B. H. J. McKellar, Nucl. Phys. **A317**, 242 (1979); S. A. Coon and M. T. Pena, Phys. Rev. C **48**, 2559 (1993); M. A. Robilotta and H. T. Coelho, Nucl. Phys. **A460**, 645 (1986).

[4] H. Witała, W. Glöckle, D. Hüber, J. Golak, and H. Kamada, Phys. Rev. Lett. **81**, 1183 (1998); R. Bieber *et al.*, *ibid.* **84**, 606 (2000); H. Sakai *et al.*, *ibid.* **84**, 5288 (2000); K. Sekiguchi *et al.*, Phys. Rev. C **70**, 014001 (2004); K. Ermisch *et al.*, *ibid.* **71**, 064004 (2005); St. Kistryn *et al.*, *ibid.* **72**, 044006 (2005).

[5] A. J. Sarty *et al.*, Phys. Rev. C **47**, 459 (1993); N. R. Kolb, P. N. Dezendorf, M. K. Brussel, B. B. Ritchie, and J. H. Smith, *ibid.* **44**, 37 (1991).

[6] R. Skibiński, J. Golak, H. Kamada, H. Witała, W. Glöckle, and A. Nogga, Phys. Rev. C **67**, 054001 (2003); R. Skibiński, J. Golak, H. Witała, W. Glöckle, H. Kamada, and A. Nogga, *ibid.* **67**, 054002 (2003).

[7] V. D. Efros, W. Leidemann, G. Orlandini, and E. L. Tomusiak, Phys. Lett. **B484**, 223 (2000).

[8] J. Golak, R. Skibiński, W. Glöckle, H. Kamada, A. Nogga, H. Witała, V. D. Efros, W. Leidemann, G. Orlandini, and E. L. Tomusiak, Nucl. Phys. **A707**, 365 (2002).

[9] V. N. Fetisov, A. N. Gorbunov, and A. T. Varfolomeev, Nucl. Phys. **71**, 305 (1965).

[10] H. M. Gerstenberg and J. S. O'Connell, Phys. Rev. **144**, 834 (1966).

[11] W. Wölfli, R. Bösch, J. Lang, R. Müller, and P. Marmier, Phys. Lett. **22**, 75 (1966).

[12] B. D. Belt, C. R. Bingham, M. L. Halbert, and A. van der Woude, Phys. Rev. Lett. **24**, 1120 (1970).

[13] S. K. Kundu, Y. M. Shin, and G. D. Wait, Nucl. Phys. **A171**, 384 (1971).

[14] A. van der Woude, M. L. Halbert, C. R. Bingham, and B. D. Belt, Phys. Rev. Lett. **26**, 909 (1971).

[15] G. Ticcioni, S. N. Gardiner, J. L. Matthews, and R. O. Owens, Phys. Lett. **B46**, 369 (1973).

[16] J. L. Matthews, T. Kruse, M. E. Williams, R. O. Owens, and W. Savin, Nucl. Phys. **A223**, 221 (1974).

[17] B. L. Berman, S. C. Fultz, and P. F. Yergi, Phys. Rev. C **10**, 2221 (1974).

[18] D. M. Skopik, H. R. Weller, N. R. Roberson, and S. A. Wender, Phys. Rev. C **19**, 601 (1979).

[19] D. D. Faul, B. L. Berman, P. Meyer, and D. L. Olson, Phys. Rev. C **24**, 849 (1981).

[20] T. Kii, T. Shima, T. Baba, and Y. Nagai, Nucl. Instrum. Methods A **552**, 329 (2005).

[21] H. Ohgaki, S. Sugiyama, T. Yamazaki, T. Mikado, M. Chiwaki, K. Yamada, R. Suzuki, T. Noguchi, and T. Tomimasu, IEEE Trans. Nucl. Sci. **38**, 386 (1991).

[22] S. C. Brown, Basic data of plasma physics (MIT press, Cambridge, Mass., 1959).

[23] B. F. Gibson and D. R. Lehman, Phys. Rev. C **13**, 477 (1976).

[24] T. Shima, S. Naito, Y. Nagai, T. Baba, K. Tamura, T. Takahashi, T. Kii, H. Ohgaki, and H. Toyokawa, Phys. Rev. C **72**, 044004 (2005).

[25] D. M. Skopik, J. Asai, D. H. Beck, T. P. Dielschneider, R. E. Pywell, and G. A. Retzlaff, Phys. Rev. C **28**, 52 (1983).

[26] H. H. Andersen and J. F. Ziegler, *Hydrogen Stopping Powers and Ranges in All Elements: Stopping and Ranges of Ions in Matter* (Pergamon Press, New York, 1977), Vol. 3; J. F. Ziegler, *Helium Stopping Powers and Ranges in All Elements: Stopping and Ranges of Ions in Matter* (Pergamon Press, New York, 1978), Vol. 4; U. Littmark and J. F. Ziegler, *Handbook of Range Distributions for Energetic Ions in All Elements: Stopping and Ranges of Ions in Matter* (Pergamon Press, New York, 1980), Vol. 4.

[27] H. Toyokawa, T. Kii, H. Ohgaki, T. Baba, T. Shima, and Y. Nagai, IEEE Trans. Nucl. Sci. **47**, 1954 (2000).

[28] T. Ohsaki, Y. Nagai, M. Igashira, T. Shima, T. S. Suzuki, T. Kikuchi, T. Kobayashi, T. Takaoka, M. Kinoshita, and Y. Nobuhara, Nucl. Instrum. Methods A **425**, 302 (1999).

[29] W. C. Barber, W. D. George, and D. D. Reagan, Phys. Rev. **98**, 73 (1955).

[30] W. E. Del Bianco and W. E. Stephens, Phys. Rev. **126**, 709 (1962).

[31] R. B. Wiringa, V. G. J. Stoks, and R. Schiavilla, Phys. Rev. C **51**, 38 (1995).

[32] B. S. Pudliner, V. R. Pandharipande, J. Carlson, S. C. Pieper, and R. B. Wiringa, Phys. Rev. C **56**, 1720 (1997).

[33] D. O. Riska, Phys. Scr. **31**, 471 (1985); **31**, 107 (1985).

[34] J. Golak, H. Kamada, H. Witała, W. Glöckle, J. Kuroś, R. Skibiński, V. V. Kotlyar, K. Sagara, and H. Akiyoshi, Phys. Rev. C **62**, 054005 (2000).

[35] V. V. Kotlyar, H. Kamada, J. Golak, and W. Glöckle, Few-Body Syst. **28**, 35 (2000).

[36] A. Deltuva, A. C. Fonseca, and P. U. Sauer, Phys. Rev. C **71**, 054005 (2005).

[37] A. Deltuva, private communications; A. C. Fonseca, Bull. Am. Phys. Soc. **50**, No. 6, 148 (2005).

[38] E. Epelbaum, W. Glöckle, and Ulf-G. Meißner, Nucl. Phys. **A747**, 362 (2005).